https://doi.org/10.3311/PPee.38675

Periodica Polytechnica Electrical Engineering and Computer Science

The Effect of Stator and Rotor Faults on the Dual-star Induction Motor Behavior

Yacine Imaouchen[1*], Samira Chekkal Ait Ouaret[2], Djamal Aouzellag[2], Kaci Ghedamsi[2]

[1] Université de Bejaia, Faculté de Technologie, Laboratoire de Génie Electrique Bejaia, 06000 Bejaia, Algérie
[2] Université de Bejaia, Faculté de Technologie, Laboratoire de Maitrise des Energies Renouvelables, 06000 Bejaia, Algérie
[*] Corresponding author, e-mail: yacine.imaouchen@univ-bejaia.dz

Received: 28 October 2024, Accepted: 03 April 2025, Published online: 24 April 2025

Abstract

Dual-star induction machines (DSIMs) are widely used in automated production systems that require uninterrupted service. As they mostly operate under dynamic real-time conditions, faults can significantly accelerate the degradation of critical components in variable-speed and load regimes. Therefore, robust monitoring algorithms are essential to assess damage levels and failure modes as faults evolve. For this purpose, a proposed approach leverages the Hilbert envelope spectrum to extract fault-related frequency components from stator current signals, providing a basis for identifying both broken rotor bar (BRB) and inter-turn short circuit (ITSC) faults. A key feature of this methodology is the use of a health indicator, derived from the current envelope spectrum to address challenges associated with damage level and load conditions from a signal processing perspective. Crucially, the relationship between the health indicator, fault severity, and load variations is statistically modeled using surface fitting. The stator current signals required for evaluating the approach are gathered from different simulations of the DSIM, subjected to various levels of damage and load conditions. The results obtained suggest that the third-order polynomial could be sufficient to model the relationship. These comprehensive analyses conclusively demonstrate the efficacy and practical applicability of the proposed fault detection approach, thus contributing significantly to the understanding of electrical machine reliability and fault mitigation.

Keywords

dual-star induction machine (DSIM), broken bar fault, interturn short-circuit fault, fault detection, surface fitting

1 Introduction

Multiphase machines, particularly dual-star induction machines (DSIM), have seen widespread adoption in industrial applications due to their intrinsic robustness and reliability. They have been recommended for various high-power sectors, such as hybrid electric vehicles, marine and locomotive propulsion, aerospace engineering, and off-shore wind energy systems, especially in contexts where environmental safety is a priority [1, 2]. These machines are frequently used in automated production systems that require continuous operation. However, their functioning in dynamic, real-time environments makes them vulnerable to various faults that can hasten the wear of critical components [3]. Effective fault management helps minimize downtime and prolong equipment lifespan, resulting in substantial cost savings. Although thermal and vibration monitoring have been standard practices for decades, recent research has predominantly focused on electrical motor monitoring, with a particular emphasis on stator current analysis [4–6]. Furthermore, while techniques like Motor Current Signature Analysis (MCSA) and wavelet transforms are widely employed for fault detection, they show limitations in adapting to different motor types and operating conditions [7, 8].

Among electrical failures, the broken rotor bar (BRB) fault has been widely studied, with causes ranging from manufacturing defects to overload conditions and mechanical fractures. When a BRB fault occurs, it can cause substantial current surges and increased stress on neighboring rotor bars. This issue is one of the most common in induction motors, representing around 8% of reported cases [9]. Razik et al. [10] developed a DSIM model with rotor faults using MCSA to evaluate fault severity. While MCSA is widely used, focusing solely on rotor faults may restrict the model's ability to detect other issues, especially in high-power applications where multiple or complex faults may arise.

Cite this article as: Imaouchen, Y., Chekkal Ait Ouaret, S., Aouzellag, D., Ghedamsi, K. "The Effect of Stator and Rotor Faults on the Dual-star Induction Motor Behavior", Periodica Polytechnica Electrical Engineering and Computer Science, 2025. https://doi.org/10.3311/PPee.38675

A more comprehensive approach that includes stator faults and other anomalies would enable more thorough diagnostics. Open-phase faults and inter-turn short circuits are two common issues in electrical machines that have been extensively researched [11, 12]. In the case of an open-phase fault, a winding connection is lost, leading to reduced power and current imbalances in the remaining phases. This results in diminished torque and excessive vibrations. On the other hand, inter-turn short circuits cause abnormal current flow due to contact between windings, which can lead to overheating. Both types of faults can have serious consequences, such as reduced torque, current imbalance, and irreversible winding damage [13, 14]. A novel diagnostic algorithm, based on the amplitude and phase angle of the interturn short fault descriptor (ITSF-FD), offers a robust solution for detecting and assessing the severity of faults in electrical machines without requiring harmonic analysis [15]. All of these faults can lead to decreased energy efficiency and increased operating costs. Understanding and addressing these issues are crucial for maintaining the reliability and longevity of electrical machines. To categorize and gauge the gravity of various electrical faults, a new squirrel cage model of the DSIM is developed in [16]. Then, a two-phase biphasic configuration was proposed to address open-phase faults. A fault-tolerant control strategy for DSIMs in marine propulsion was proposed in [17]. While promising, experimental validation would strengthen the conclusions. Other studies [4, 18] explored fault diagnosis using fast Fourier transform (FFT) and wavelet transform. Despite being effective for frequency analysis, FFT faces challenges with non-stationary signals. Wavelet transform, better for time-varying signals, requires computational resources.

Thus, non-invasive fault diagnosis has emerged as a preferred approach due to its reliance on stator voltage or current waveforms, effectively eliminating the need for additional sensors. This method is particularly advantageous for detecting internal faults, which are primarily identified through indices extracted from stator line currents. Despite these developments, there remains a significant gap in research concerning multi-phase induction motors. Few studies have examined the applicability of existing techniques and indices to multi-phase motors, highlighting the need for further investigation. By using spectral analysis of the stator current a diagnosis technique is proposed in [19] but requires long sampling durations and lacks specific fault signatures. A statistical method for stator interturn fault detection is developed in [20], and an adaptive neuro-fuzzy inference systems (ANFIS) approach for stator winding incipient fault detection is investigated in [21], but require accurate training of the ANFIS. A winding function method incorporating magnetic saturation and spectral analysis was introduced in [22] but also faces similar limitations. In [23], a quantitative index known as the current trajectory mass center has been extracted and used to detect the stator interturn fault. Nonetheless, the impact of load level changes on fault detection and the sensitivity of these methods to fault severity has not been explored in [19–23].

This paper presents a comprehensive diagnostic evaluation of DSIM, widely employed in high-power and critical applications. The study examines the effects of two common fault conditions: broken rotor bars (BRB) and inter-turn short circuits (ITSC). A detailed mathematical model was developed to simulate DSIM behavior under these faults, analyzing their impact on motor performance parameters. Stator current signals were obtained from simulations under varying fault severities and operational loads. A fault detection methodology is proposed, utilizing signal processing techniques such as the Hilbert envelope spectrum to extract fault-related frequency components. The study also employs a surface fitting model to analyze the relationship between fault severity, load variations, and a health indicator derived from stator current outputs.

2 Theoretical analyses

2.1 Dynamic modelling of the DSIM

In modelling the DSIM, the following assumptions were adopted:

1. uniform air gap,
2. negligible saturation,
3. sinusoidal distribution of stator windings,
4. naturally isolated stator windings and,
5. negligible inter-bar current.

The squirrel cage rotor is modeled using an equivalent circuit composed of (N_r + 1) meshes, as depicted in Fig. 1.

Each mesh is represented by an equivalent circuit comprising a rotor bar and an end-ring segment, characterized by resistive and inductive properties (R_b, R_e, L_b, L_e). Here, R_b and L_b denote the resistance and inductance of the rotor bar, respectively, while R_e and L_e represent the resistance and inductance of the end-ring segment. The rotor voltage equations for the N_r loops can be expressed as follows:

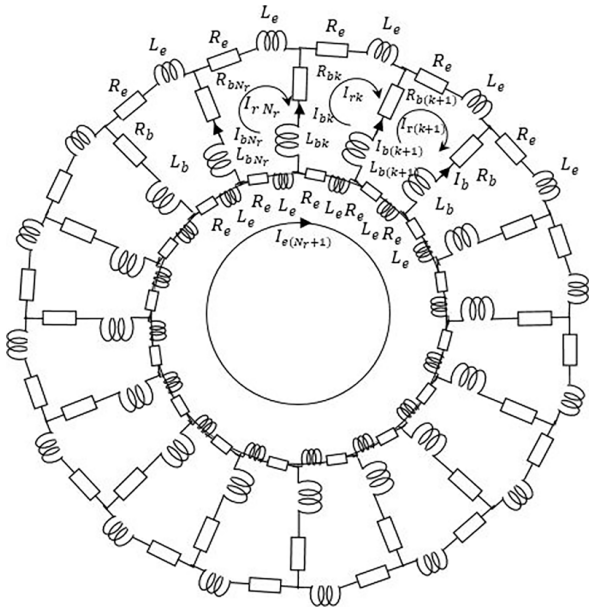

Fig. 1 The equivalent circuit of the rotor squirrel-cage

$$\begin{aligned}&\left(2R_{ek}+R_{b(k+1)}+R_{bk}\right)\cdot I_{bk}-R_{bk}\cdot I_{r(k-1)}\\&-R_{b(k+1)}\cdot I_{r(k+1)}-R_e\cdot I_{e(N_r+1)}+\frac{d\psi_{rk}}{dt}=0,\end{aligned}\tag{1}$$

where, ψ_{rk} is the rotor flux crossing the rotor loop k.

The voltage equations of DSIM can be expressed in the form:

$$\begin{cases}\left[V_{s1}\right]=\left[R_{s1}\right]\left[I_{s1}\right]+\dfrac{\left[d\psi_{s1}\right]}{dt}\\ \left[V_{s2}\right]=\left[R_{s2}\right]\left[I_{s2}\right]+\dfrac{\left[d\psi_{s2}\right]}{dt},\\ \left[V_r\right]=\left[R_r\right]\left[I_r\right]+\dfrac{\left[d\psi_r\right]}{dt}\end{cases}\tag{2}$$

where the stator and rotor flux are defined as:

$$\begin{cases}\left[\psi_{s1}\right]=\left[L_{s1,s1}\right]\left[I_{s1}\right]+\left[L_{s1,s2}\right]\left[I_{s2}\right]+\left[L_{s1,r}\right]\left[I_r\right]\\ \left[\psi_{s2}\right]=\left[L_{s2,s2}\right]\left[I_{s2}\right]+\left[L_{s2,s1}\right]\left[I_{s1}\right]+\left[L_{s2,r}\right]\left[I_r\right],\\ \left[\psi_r\right]=\left[L_{r,r}\right]\left[I\right]+\left[L_{r,s1}\right]\left[I_{s1}\right]+\left[L_{r,s2}\right]\left[I_{s2}\right]\end{cases}\tag{3}$$

with:

$$\left[V_{s1(2)}\right]=\left[v_{as1(2)}\quad v_{bs1(2)}\quad v_{cs1(2)}\right]^t,$$

$$\left[I_{s1(2)}\right]=\left[i_{as1(2)}\quad i_{bs1(2)}\quad i_{cs1(2)}\right]^t,$$

$$\left[\psi_{s1(2)}\right]=\left[\psi_{as1(2)}\quad \psi_{bs1(2)}\quad \psi_{cs1(2)}\right]^t,$$

$$\left[V_r\right]=\left[v_{r1}\ v_{r2}\ v_{r3}\cdots\ v_{rj}\cdots\ v_{rN_r}\right]^t,$$

$$\left[I_r\right]=\left[i_{r1}\ i_{r2}\ i_{r3}\cdots\ i_{rj}\cdots\ i_{rN_r}\right]^t,$$

$$\left[\psi_r\right]=\left[\psi_{r1}\ \psi_{r2}\ \psi_{r3}\cdots\ \psi_{rj}\cdots\ \psi_{rN_r}\right]^t,$$

$$\left[R_{s1(2)}\right]=\operatorname{diag}\left(\left[r_{as1(2)}\ r_{bs1(2)}\ r_{cs1(2)}\right]\right),$$

$$\left[L_{s1,s1}\right]=\left[L_{s2,s2}\right]=\begin{bmatrix}l_{fs}+l_{ms} & \dfrac{-l_{ms}}{2} & \dfrac{-l_{ms}}{2}\\ \dfrac{-l_{ms}}{2} & l_{fs}+l_{ms} & \dfrac{-l_{ms}}{2}\\ \dfrac{-l_{ms}}{2} & \dfrac{-l_{ms}}{2} & l_{fs}+l_{ms}\end{bmatrix},$$

$$\left[L_{s1,s2}\right]=\left[L_{s2,s1}\right]$$
$$=l_{ms}\begin{bmatrix}\cos(\alpha) & \cos(\alpha+2\pi/3) & \cos(\alpha+4\pi/3)\\ \cos(\alpha+4\pi/3) & \cos(\alpha) & \cos(\alpha+2\pi/3)\\ \cos(\alpha+2\pi/3) & \cos(\alpha+4\pi/3) & \cos(\alpha)\end{bmatrix},$$

$$\left[R_r\right]=\begin{bmatrix}R_{rr} & -R_b & 0 & \cdots & -R_b & -R_e\\ -R_b & R_{rr} & -R_b & \cdots & 0 & -R_e\\ \vdots & -R_b & \ddots & \cdots & \vdots & -R_e\\ \vdots & \vdots & \vdots & \ddots & -R_b & \vdots\\ -R_b & 0 & \vdots & \cdots & R_{rr} & -R_e\\ -R_e & -R_e & -R_e & \cdots & -R_e & N_rR_e\end{bmatrix},$$

where: $R_{rr} = 2(R_b + R_e)$; l_{fs} and l_{rr} are stator and rotor leakage inductors, respectively. l_{ms} and l_{mb} are the maximum stator and rotor magnetization inductors, respectively. $m_{sr}=\sqrt{l_{ms}\cdot l_{mb}}$ is the maximum mutual inductance between stator phase and corresponding rotor phase. Also, the coupling inductance matrices between star1 and rotor and vice versa are given by: $[L_{r,s1}] = [L_{s1,r}]^t$.

$$\left[L_{r,r}\right]=\begin{bmatrix}l_{mr}+2(L_b+L_e) & l_{r1r2}-L_b & \cdots & l_{r1r(N_r-1)} & l_{r1rN_r-L_b} & -L_e\\ l_{r2r1}-L_b & l_{mr}+2(L_b+L_e) & \cdots & l_{r2r(N_r-1)} & l_{r2rN_r} & -L_e\\ \vdots & \vdots & \vdots & \vdots & \vdots & \vdots\\ \vdots & \vdots & \ddots & l_{mr}+2(L_b+L_e) & l_{r(N_{r-1})rN_r}-L_b & \vdots\\ l_{r(N_r-1)r1}-L_b & l_{rN_rr2}-L_b & \cdots & l_{rN_rr(N_{r-1})}-L_b & l_{mr}+2(L_b+L_e) & -L_e\\ -L_e & -L_e & \cdots & -L_e & -L_e & N_rL_e\end{bmatrix},\tag{4}$$

Similarly, the coupling inductance matrices between 2nd star and rotor, and vice versa, are $[L_{r,s2}] = [L_{s2,r}]^t$.

The details of the submatrices $[L_{r,r}] = [L_{s1,r}]$, and $[L_{s2,r}]$ are given in the Eqs. (4), (5) and (6).

$$[L_{s1,r}] = m_{sr}\begin{bmatrix} \cos\left(\theta_r+\frac{\pi}{N_r}\right) & \cos\left(\theta_r+\frac{3\pi}{N_r}\right) & \cos\left(\theta_r+\frac{5\pi}{N_r}\right)\cdots & \cos\left(\theta_r+\frac{(2N_r-1)\pi}{N_r}\right) & 0 \\ \cos\left(\theta_r+\frac{\pi}{N_r}-\frac{2\pi}{3}\right) & \cos\left(\theta_r+\frac{3\pi}{N_r}-\frac{2\pi}{3}\right) & \cos\left(\theta_r+\frac{5\pi}{N_r}-\frac{2\pi}{3}\right)\cdots & \cos\left(\theta_r+\frac{(2N_r-1)\pi}{N_r}-\frac{2\pi}{3}\right) & 0 \\ \cos\left(\theta_r+\frac{\pi}{N_r}+\frac{2\pi}{3}\right) & \cos\left(\theta_r+\frac{3\pi}{N_r}+\frac{2\pi}{3}\right) & \cos\left(\theta_r+\frac{5\pi}{N_r}+\frac{2\pi}{3}\right) & \cos\left(\theta_r+\frac{(2N_r-1)\pi}{N_r}+\frac{2\pi}{3}\right) & 0 \end{bmatrix}, \quad (5)$$

$$[L_{s2,r}] = m_{sr}$$

$$\begin{bmatrix} \cos\left(\theta_r-\alpha+\frac{\pi}{N_r}\right) & \cos\left(\theta_r-\alpha+\frac{3\pi}{N_r}\right) & \cos\left(\theta_r-\alpha+\frac{5\pi}{N_r}\right)\cdots & \cos\left(\theta_r-\alpha+\frac{(2N_r-1)\pi}{N_r}\right) & 0 \\ \cos\left(\theta_r-\alpha+\frac{\pi}{N_r}-\frac{2\pi}{3}\right) & \cos\left(\theta_r-\alpha+\frac{3\pi}{N_r}-\frac{2\pi}{3}\right) & \cos\left(\theta_r-\alpha+\frac{5\pi}{N_r}-\frac{2\pi}{3}\right)\cdots & \cos\left(\theta_r-\alpha+\frac{(2N_r-1)\pi}{N_r}-\frac{2\pi}{3}\right) & 0 \\ \cos\left(\theta_r-\alpha+\frac{\pi}{N_r}+\frac{2\pi}{3}\right) & \cos\left(\theta_r-\alpha+\frac{3\pi}{N_r}+\frac{2\pi}{3}\right) & \cos\left(\theta_r-\alpha+\frac{5\pi}{N_r}+\frac{2\pi}{3}\right)\cdots & \cos\left(\theta_r-\alpha+\frac{(2N_r-1)\pi}{N_r}+\frac{2\pi}{3}\right) & 0 \end{bmatrix}. \quad (6)$$

The mathematical expressions of the electromagnetic torque T_{em} and the rotor velocity Ω_r are represented by the Eqs. (7) and (8) as follows:

$$T_{em} = p\left([I_{s1}]^t \frac{d}{d\theta_r}[L_{s1,r}][I_r] + [I_{s2}]^t \frac{d}{d\theta_r}[L_{s2,r}][I_r]\right), \quad (7)$$

$$J\frac{d\Omega_r}{dt} = T_{em} - T_r - K_f\Omega_r, \quad (8)$$

where: p is the pair poles number, J is the total inertia, K_f is the viscous friction and Ω_r is the rotor velocity.

2.1.1 The DSIM under BRB fault

In order to simulate the DSIM under BRB fault, the k broken bar resistance is strongly increased by an additional resistance R_{bF} called the defect resistance. Consequently, the resistance matrix R_r of the rotor squirrel cage is changed taking into account the additional defect resistance matrix R_{dF}. So, the faulty resistance matrix R_{rF} is then defined by: $[R_{rF}] = [R_r] + [R_{dF}]$.

The additional defect resistance matrix R_{dF} is expressed by:

$$[R_{dF}] = \begin{bmatrix} 0 & \cdots & 0 & 0 & \cdots & 0 \\ \vdots & \cdots & \vdots & \vdots & \cdots & \vdots \\ 0 & \cdots & 0 & 0 & \cdots & 0 \\ 0 & 0 & R_{bF_k} & -R_{bF_k} & \cdots & 0 \\ 0 & 0 & -R_{bF_k} & R_{bF_k} & \cdots & \vdots \\ \vdots & \vdots & \vdots & \vdots & \vdots & \vdots \\ 0 & \cdots & 0 & 0 & \cdots & 0 \end{bmatrix}. \quad (9)$$

The curves for speed, electromagnetic torque, stator and rotor currents versus time are plotted with a constant nominal load of 100 Nm applied at 1.5 s. Subsequently, a bar failure is considered to occur at t = 3 s, followed by a second bar failure at t = 4 s, and a third bar failure also at t = 4 s, as illustrated in Fig. 2. Analyzing these parameters and events assesses how the machine responds to disturbances.

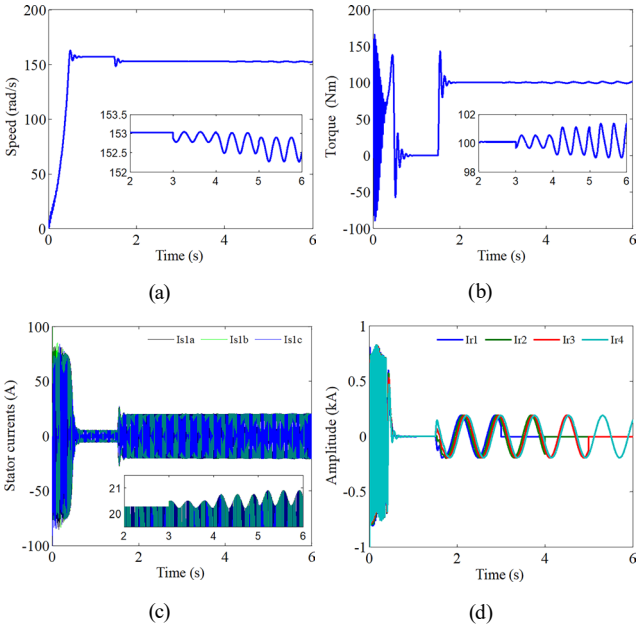

Fig. 2 The DSIM performances under BRB fault (a) rotating speed, (b) electromagnetic torque, (c) stator currents of the 1st star, and (d) Rotor currents

The results demonstrate the significant impact of three adjacent broken bars on machine performance. A single broken bar initially causes a minor modulation in the stator current, but this modulation becomes more pronounced as the number of broken bars increases. Additionally, both torque and rotational speed exhibit slight fluctuations when the first rotor bar breaks, and these fluctuations intensify with subsequent faults.

2.1.2 The DSIM under ITSC fault

An ITSC fault is characterized by the existence of an additional circuit branch between the turns of as_1-phase in the stator winding configuration as shown in Fig. 3. The *dq* model offers a simplified representation of balanced AC machines. However, the asymmetries inherent in ITSF render it inadequate. Despite its increased complexity, the natural frame model is thus required.

To design a suitable system, we've made several simplifying assumptions: a fault occurred in the stator winding of phase (a_s) in the first star connection, the resistance (r_{f1}) is treated as a fault resistance ($r_{f1} = 0$), the phase voltage (a_s) of the first star connection is considered to be the sum of the two voltages.

Assuming N_s as the total number of turns at healthy state which is the same for all phases and N_{ccn} the number of the short-circuited turns for the *i*-phase, then $N_s = N_n = N_{ccn}$, where N_n is the number of useful turns for after the short-circuit. Therefore, the ratio between the number of short-circuited turns and the total number of turns is given by:

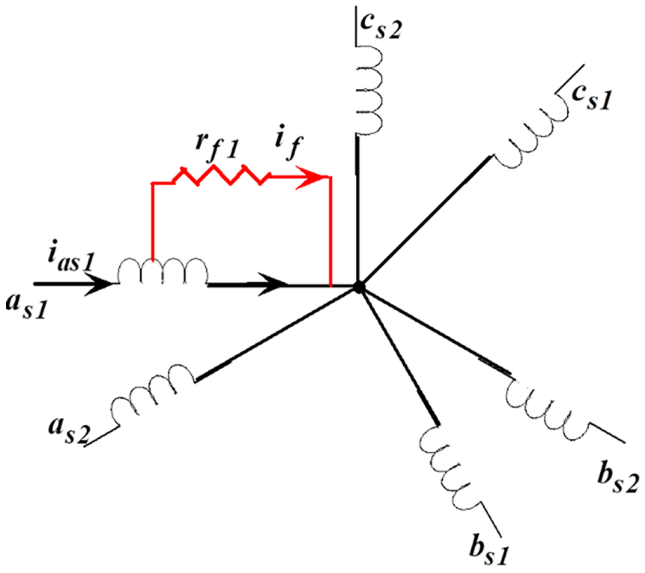

Fig. 3 Diagram illustrating the two stator windings of the studied DSIM with a short circuit occurring in its a_{s1} phase

$$\mu = \frac{N_{ccn}}{N_s}. \tag{10}$$

Consequently, the inductance and resistance matrices are modified to incorporate the coefficients of the short-circuited turns. As a result, the faulty matrices for $[R_{s1}]$, $[L_{s1,s1}]$, $[L_{s1,s2}]$ and $[L_{s1,r}]$ are represented by Eqs. (11–14).

$$[R_{s1}] = \begin{bmatrix} r_{as1} & 0 & 0 & -r_{f1} \\ 0 & r_{bs1} & 0 & 0 \\ 0 & 0 & r_{cs1} & 0 \\ -r_{f1} & 0 & 0 & r_{sc} \end{bmatrix}, \tag{11}$$

where: $r_{as1} = (1-\mu)\cdot r_{s1} + r_f$; $r_{sc} = \mu\, r_{s1} + r_{f1}$.

$$[L_{s1,s1}] = l_{s1}\begin{bmatrix} (1-\mu)^2 & 0 & 0 & 0 \\ 0 & 1 & 0 & 0 \\ 0 & 0 & 1 & 0 \\ 0 & 0 & 0 & \mu^2 \end{bmatrix}$$

$$+l_{ms}\begin{bmatrix} (1-\mu)^2 & \frac{-(1-\mu)}{2} & \frac{-(1-\mu)}{2} & \mu(1-\mu) \\ \frac{-(1-\mu)}{2} & 1 & \frac{-1}{2} & \frac{-\mu}{2} \\ \frac{-(1-\mu)}{2} & \frac{-1}{2} & 1 & \frac{-\mu}{2} \\ \mu(1-\mu) & \frac{-\mu}{2} & \frac{-\mu}{2} & \mu^2 \end{bmatrix}. \tag{12}$$

To investigate ITSC faults at rates of 5%, 15% and 25%, simulations were conducted by intentionally inducing short circuits on the first phase winding only, assuming a fault resistance of zero. Initially, we assumed a healthy machine operating under normal conditions.

At t = 1.5 s, a half-nominal load torque of 50 Nm was applied. ITSC fault was then introduced at t = 3 s and its severity increased incrementally every second. Fig. 4 depicts the electromechanical behavior of the DSIM as reflected in its rotational speed, electromagnetic torque, stator and rotor currents.

As expected, the faulted phase exhibits a substantial increase in current amplitude, while the other phases also experience a noticeable rise in current amplitude (Fig. 4 (c)). In parallel, the electromagnetic torque, the speed and the rotor currents reveal ripples upon the

$$\left[L_{s1,s2}\right]=l_{ms}\begin{bmatrix}(1-\mu)\cos(\alpha) & (1-\mu)\cos\left(\alpha+\frac{2\pi}{3}\right) & (1-\mu)\cos\left(\alpha+\frac{4\pi}{3}\right)\\ \cos\left(\alpha+\frac{4\pi}{3}\right) & \cos(\alpha) & \cos\left(\alpha+\frac{2\pi}{3}\right)\\ \cos\left(\alpha+\frac{2\pi}{3}\right) & \cos\left(\alpha+\frac{4\pi}{3}\right) & \cos(\alpha)\\ (\mu)\cos(\alpha) & (\mu)\cos\left(\alpha+\frac{2\pi}{3}\right) & (\mu)\cos\left(\alpha+\frac{4\pi}{3}\right)\end{bmatrix}, \tag{13}$$

$$\left[L_{s1,r}\right]=m_{sr}\begin{bmatrix}(1-\mu)\cos\left(\theta_r+\frac{\pi}{N_r}\right) & (1-\mu)\cos\left(\theta_r+\frac{3\pi}{N_r}\right) & (1-\mu)\cos\left(\theta_r+\frac{5\pi}{N_r}\right)\cdots & (1-\mu)\cos\left(\theta_r+\frac{(2N_r-1)\pi}{N_r}\right) & 0\\ \cos\left(\theta_r+\frac{\pi}{N_r}-\frac{2\pi}{3}\right) & \cos\left(\theta_r+\frac{3\pi}{N_r}-\frac{2\pi}{3}\right) & \cos\left(\theta_r+\frac{5\pi}{N_r}-\frac{2\pi}{3}\right)\cdots & \cos\left(\theta_r+\frac{(2N_r-1)\pi}{N_r}-\frac{2\pi}{3}\right) & 0\\ \cos\left(\theta_r+\frac{\pi}{N_r}+\frac{2\pi}{3}\right) & \cos\left(\theta_r+\frac{3\pi}{N_r}+\frac{2\pi}{3}\right) & \cos\left(\theta_r+\frac{5\pi}{N_r}+\frac{2\pi}{3}\right)\cdots & \cos\left(\theta_r+\frac{(2N_r-1)\pi}{N_r}+\frac{2\pi}{3}\right) & 0\\ \mu\cos\left(\theta_r+\frac{\pi}{N_r}\right) & \mu\cos\left(\theta_r+\frac{3\pi}{N_r}\right) & \mu\cos\left(\theta_r+\frac{5\pi}{N_r}\right)\cdots & \mu\cos\left(\theta_r+\frac{(2N_r-1)\pi}{N_r}\right) & 0\end{bmatrix}. \tag{14}$$

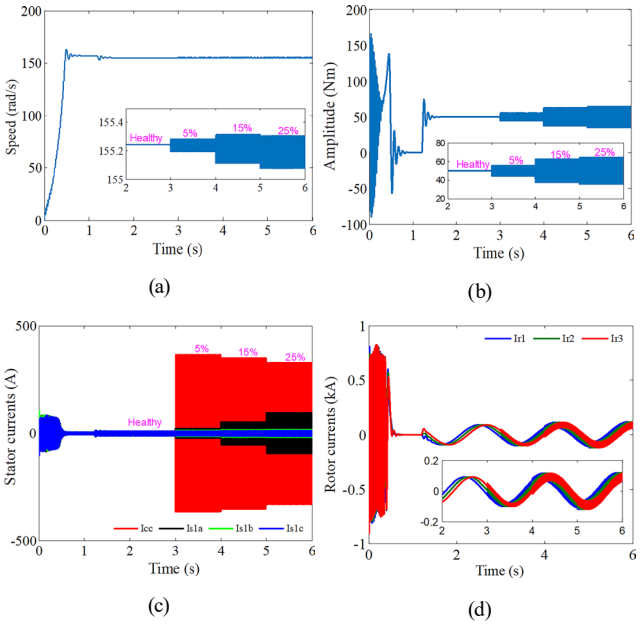

Fig. 4 The DSIM performances under ITSC fault (a) rotating speed, (b) electromagnetic torque, (c) stator currents of the 1st star, and (d) Rotor currents

occurrence of the ITSC fault. These ripples become more pronounced as the fault severity grows.

2.2 Proposed diagnosis methodology

Predictive maintenance (PM) is a prominent strategy for detecting DSIM faults. It involves utilizing equipment assessment techniques, like electrical signature analysis, to proactively schedule maintenance tasks. By continuously monitoring key machine condition parameters, PM enables early detection of performance degradation or incipient failures. So, this work consists in developing a fault detection technique based on monitoring an appropriate health indicator. It is defined from measurable output currents, which reflect the fault behavior in the machine.

2.2.1 Signal envelope spectrum

Motor current signature analysis (MCSA) is widely employed to detect rotor and stator faults in induction machines. It is well-established that rotor asymmetry yields a current component at $(1 \pm 2s)f_s$, while electrical or magnetic stator asymmetry produces a component at $-f_s$ (i.e., a negative sequence component) [24]. These components induce torque ripples at frequencies of $2sf_s$ and $2f_s$, respectively, resulting in speed ripples of varying amplitudes that are differentially filtered by the machine's load inertia. The envelope of the defective motor current, modulated by the supply voltage frequency, contains fault-related frequencies. The Hilbert transform is used to extract the envelope spectrum. For a real-time signal $x(t)$, the Hilbert transform is defined as:

$$h(t)=\frac{1}{\pi}\int_{-\infty}^{+\infty}\frac{x(\tau)}{t-\tau}d\tau. \tag{15}$$

For a modulated signal $x(t)$, it is often appropriate to use the analytical signal defined by:

$$z(t) = x(t) + jh(t) = |A(t)|e^{j\theta(t)}. \quad (16)$$

Then, its amplitude can be expressed as:

$$|A(t)| = \sqrt{x^2(t) + h^2(t)}. \quad (17)$$

To evaluate the effectiveness of the Hilbert Envelope, stator current spectra of the considered machine were analyzed under three conditions: healthy, BRB fault, and ITSC fault. As illustrated in Fig. 5 (a), the amplitude of the modulated sidebands $(1 \pm 2ks)f_s$ in the current spectrum increases directly with the severity of the BRB fault. Conversely, Fig. 5 (b) demonstrates that the amplitude of the frequency $3f_s$ in the current spectrum is directly correlated with the severity of the ITSC fault.

As expected, the amplitude at the frequency $2ksf_s$ of the demodulated stator current signal using Hilbert transform increases proportionally to the BRB fault severity, (Fig. 5 (c)). Moreover, the demodulated stator current signal of the machine with an ITSC fault in Fig. 5 (d) reveals an increase in the amplitude of the frequency $3f_s$.

2.2.2 Principle underlying the proposed method

Obviously, the application of MCSA to DSIM fault detection presents unique challenges. Each fault induces specific frequency components, known as fault patterns.

These include the characteristics of speed variations and cases where several fault patterns coincide at the same frequency, requiring further analysis to differentiate fault effects. For this purpose, a health indicator is proposed, based on the fault signatures detected by the current envelope spectrum.

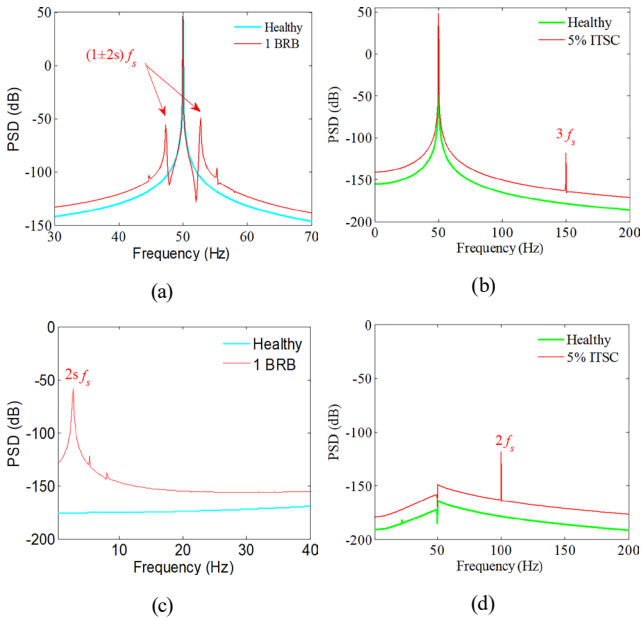

Fig. 5 Spectral analysis of the DSIM stator current under fault conditions (a) current spectrum under BRB fault, (b) current spectrum under ITSC fault, (c) current envelope spectrum under BRB fault, and (d) current envelope spectrum under ITSC fault

The application of MCSA to DSIM fault detection presents unique challenges. Each fault induces specific frequency components, or fault signatures. These include speed variations and instances where multiple fault signatures coincide at the same frequency, necessitating further analysis to differentiate between fault effects. To address this, a healthy indicator is proposed, based on the fault signatures detected in the current envelope spectrum. The procedure of the proposed diagnosis approach is shown in Fig. 6.

The proposed methodology is straightforward and accessible, since it does not require detailed prior knowledge of the motor's structure. Furthermore, its algorithm is lightweight, and the results are easily interpretable.

3 Evaluation of the proposed diagnosis method

3.1 Description of the used data

The DSIM model is used to generate data for a range of scenarios involving combinations of BRB and ITSC faults of varying severity, and diverse loading conditions. The specific combinations of these parameters are detailed in Table 1. For each load level of the DSIM, different faults

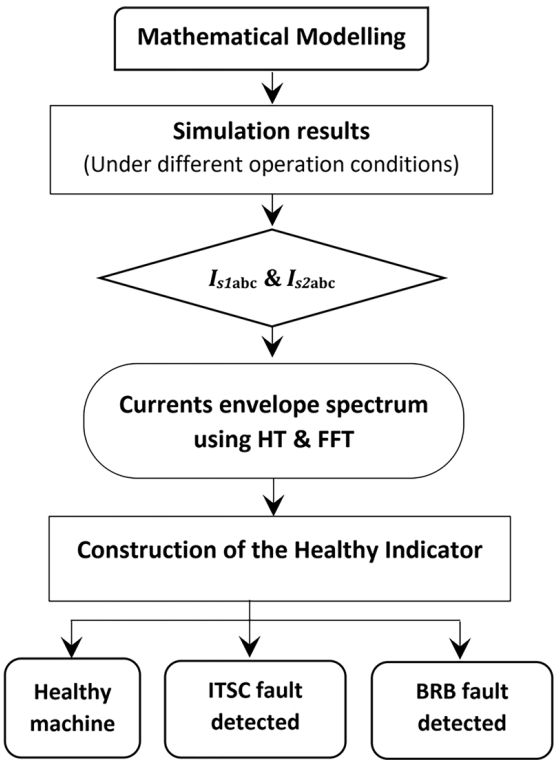

Fig. 6 Flowchart for the proposed diagnosis approach

Table 1 Stator and rotor faults and loading percentage in various scenarios

Headline	Headline
BRB fault severity (%)	0, 1, 2 or 3 broken bars (38 total bars)
Loading condition (%)	10 %, 25 %, 40 %, 60 %, 100 % (full load)
ITSC fault severity (%)	5 %, 10 %, 15 %, 20 %, 25 %, 30 %
Loading condition (%)	10 %, 20 %, 30 %, 40 %, 50 % (half load)

severities are applied and the phase currents are gathered to achieve the detection procedure. These cases provide (4 × 5) + (6 × 5) = 50 different scenarios, which can fully describe the real operating conditions of the DSIM.

3.2 Results and discussions

Table 2 presents the normalized values of the proposed HI computed for the stator current outputs of the DSIM under BRB fault conditions. The proposed HI is calculated as described in subsection 3.2.1. Additionally, Table 3 shows the normalized values of the proposed HI computed for the stator current outputs of the DSIM under ITSC fault conditions. From these results, two bar graphics are drown to illustrate the behavior of the proposed HI against the occurrence of the BRB and ITSC faults, as exposed in Figs. 7 and 8, respectively.

At first glance, these results show an increasing trend in the values of the proposed HI from the healthy case to maximums of the two faults severities, in all of the loading cases, and the proposed HI for every faulty condition is higher than in healthy ones. Moreover, the proposed

Table 2 Obtained results of normalized HI as function of BRB fault level under varying load

BRB Fault ratio	Load (Nm)				
	10	25	40	60	100
0/38	0.00025	0.00062	0.00031	0.00029	0.00081
1/38	0.10643	0.19965	0.26193	0.31843	0.40777
2/38	0.18956	0.32800	0.44043	0.65053	0.91393
3/38	0.20770	0.36776	0.47550	0.77100	1

Table 3 Obtained results of normalized HI as function of ITSC fault level under varying load

ITSC fault ratio	Load (Nm)				
	10	20	30	40	50
5	0.33341	0.32575	0.31568	0.30683	0.29777
10	0.60121	0.58838	0.57425	0.55524	0.53795
15	0.79995	0.78033	0.76241	0.73859	0.71327
20	0.93325	0.90826	0.88465	0.85970	0.82681
25	1	0.97151	0.94381	0.91581	0.87847
30	0.99538	0.96479	0.93502	0.90288	0.86336

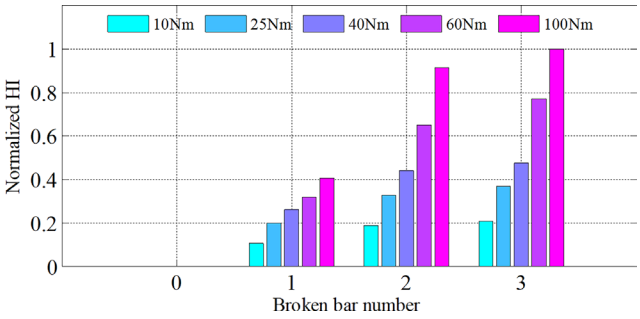

Fig. 7 Obtained results of normalized HI as function of BRB fault level under varying load

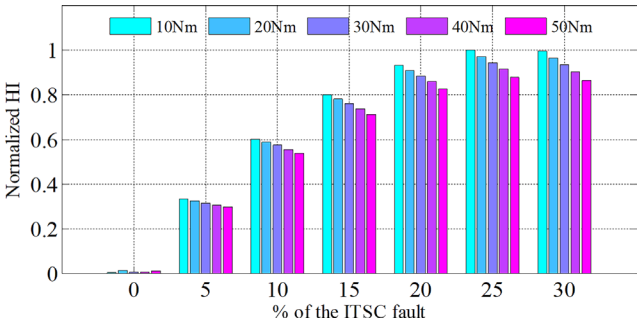

Fig. 8 Obtained results of normalized HI as function of ITSC fault level under varying load

HI values are observed to increase with varying loads for each severity of the BRB fault. However, they exhibit a decreasing trend when dealing with ITSC faults.

3.3 Surface fitting illustrating the effect of fault level and load on the proposed health indicator

At this stage, our methodology involves analyzing pairs of defect level and load data points corresponding to the proposed HI parameter. The objective is to derive a mathematical model of the form f (defect level, load) that can accurately reproduce the HI values. Polynomial regression is utilized as a surface fitting technique to determine the functional form of this relationship. A polynomial surface model, specifically the "polyij" function in MATLAB [25], was used to fit the proposed HI surface. The model incorporates polynomial terms of load and defect level, with degrees i and j respectively. Within MATLAB's constraints, the maximum degree for both i and j was limited to five. The overall polynomial degree of the fitted surface is determined by the higher of i and j.

Three metrics were employed to assess the quality of the surface fit: the coefficient of determination (R^2), the adjusted R^2, and the root mean squared error (RMSE). The R-squared (R^2) measures the model's ability to explain the variation of the data and is calculated as the ratio of the sum of squares of the regression (SSR) and the total sum of squares (SST) [26].

$$SSR = \sum_{i=1}^{n} w_i \left(\hat{y} - \bar{y}\right)^2, \tag{18}$$

$$\mathrm{SST} = \sum_{i=1}^{n} w_i \left(y_i - \bar{y}\right)^2, \tag{19}$$

$$R^2 = \frac{\mathrm{SSR}}{\mathrm{SST}}. \tag{20}$$

Here y_i is the observed data value, $\hat{y}$ is the predicted value from the fitting curve, $\bar{y}$ is the mean of the observed data and w_i is the weighting applied to each data point, usually $w_i = 1$. *R*-squared can range from 0 to 1, where values closer to 1 suggest that the model explains a larger proportion of the variation in the data.

The adjusted *R*-squared (R^2_{adj}) corrects R^2 based on the residual degrees of freedom *v*, that is defined as the difference between *n* the number of response values and *m* the number of fitted coefficients. The R^2_{adj} can take on any value less than or equal to 1, with a value closer to 1 indicating a better fit. Assuming that SSE (Sum of squares due to error) is the difference between the SST and SSR (SST = SSR + SSE), so the R^2_{adj} is calculated as follows:

$$R^2 = 1 - \frac{\mathrm{SSE}\left(n-1\right)}{\mathrm{SST}\left(v\right)}. \tag{21}$$

RMSE (Root Mean Squared Error) is the standard error of the regression and an estimate of the standard deviation of the random component in the data (Eq. (22)). A RMSE value closer to 0 indicates a fit that is more useful for prediction.

$$\mathrm{RMSE} = \sqrt{\mathrm{MSE}}, \tag{22}$$

where MSE is the mean square error or the residual mean square (MSE = SSE/*v*).

To obtain the optimal surface fitting for the construction of the proposed HI surface, all combinations of *i* and *j* values in the polynomial surface model '*polyij*' were tested. The performance of each polynomial surface model was then evaluated using the three evaluation parameters including R^2, R^2_{adj} and RMSE.

A polynomial surface fit was applied to model the proposed HI as a function of BRB fault and load levels, as depicted in Fig. 9. As it can be seen from the graphical representation of the investigated data in Table 2, the best polynomial surface fitting is obtained for third order of polynomial model (Fig. 9). Also, second-order polynomial surface fit was employed to model the proposed HI as a function of ITSC fault and load levels. As illustrated in Fig. 10, this model effectively captures the relationship between these variables based on the investigated data in Table 3.

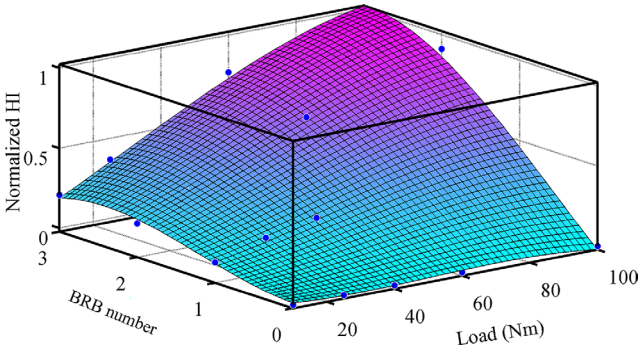

Fig. 9 3D surface plot exhibiting the effect of the load and the BRB damage level on the proposed HI

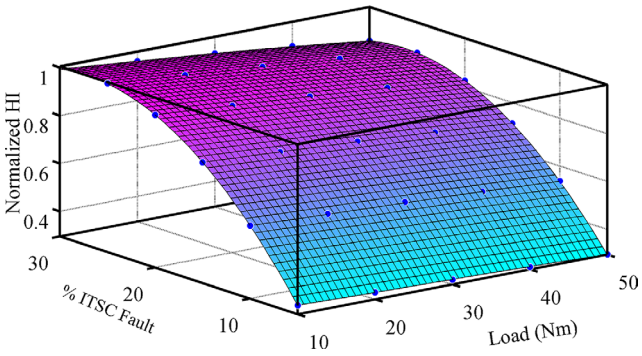

Fig. 10 3D surface plot exhibiting the effect of the load and the ITSC damage level on the proposed HI

Furthermore, the optimal polynomial model in BRB fault study is "*poly*33", i.e., $i = 3$ and $j = 3$, while "*poly*22", i.e., $i = 2$ and $j = 2$ is sufficient in ITSC fault study. Thus, R^2, R^2_{adj}, and RMSE of the optimal surface fitting models are given in the Table 4. Based on the considered polynomial orders, the model showed remarkable robustness in fitting the proposed HI values, providing an accurate representation of the data.

Fig. 11 presents the residuals plot for the developed polynomial models. These visual representations allow for an evaluation of the models fit to the data, the distribution of residuals, and the identification of potential outliers. Residuals were calculated as the difference between the observed HI values and their corresponding fitted values from the polynomial surface model. As shown in Fig. 11, the residuals appear to be randomly scattered around zero, indicating that the polynomial models are unbiased and provides a good fit to the data.

Table 4 Values of the performance metrics evaluating the polynomial surface models

	R^2	R^2_{adj}	RMSE
BRB fault case (polly33)	0.9917	0.9842	0.03843
ITSC fault case (polly22)	0.9999	0.9999	0.00259

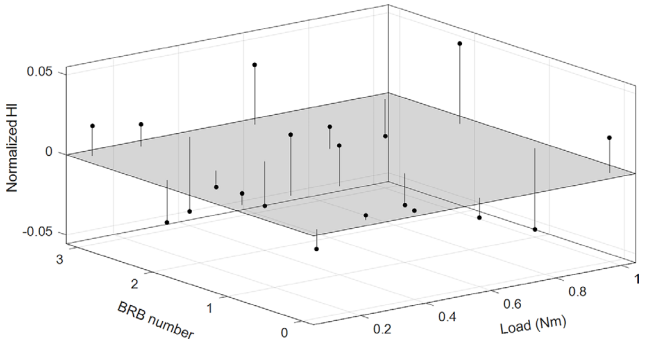

(a)

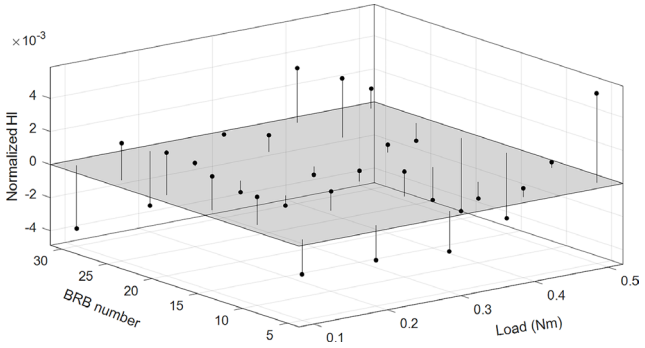

(b)

Fig. 11 Residuals plots for the obtained polynomial models developed (a) in Fig. 10, and (b) in Fig. 11

4 Conclusion

This paper investigates fault detection in dual-star induction machines by modelling the effects of broken rotor bar and inter-turn short circuit faults. The results of this study underscore the accuracy and robustness of the proposed fault detection technique for DSIMs. The key achievement lies in the statistical modeling of a health indicator (HI), which effectively characterizes the severity of both broken rotor bar (BRB) and inter-turn short circuit (ITSC) faults. Simulation results indicate that a third-order polynomial model accurately fits the HI for BRB faults ($R^2 = 0.9917$), while a second-order polynomial adequately represents the HI for ITSC faults ($R^2 = 0.9999$). These high R^2 values confirm the model's robustness in fitting the HI, providing an accurate representation of the data. The comprehensive evaluations confirm the practical applicability of this methodology, significantly enhancing the understanding of DSIM reliability and contributing to improved fault mitigation strategies. Ultimately, this work lays the foundation for future advances in the monitoring and maintenance of electrical machines, promoting operational efficiency and longevity.

References

[1] Levi, E. "Multiphase electric machines for variable-speed applications", IEEE Transactions on Industrial Electronics, 55(5), pp. 1893–1909, 2008. https://doi.org/10.1109/TIE.2008.918488

[2] Chekkal, S., Lahaçani, N. A., Aouzellag, D., Ghedamsi, K. "Fuzzy logic control strategy of wind generator based on the dual-stator induction generator", International Journal of Electrical Power and Energy Systems, 59, pp. 166–175, 2014. https://doi.org/10.1016/j.ijepes.2014.02.005

[3] Foito, D., Maia, J., Fernão Pires, V., Martins, J. F. "Double three-phase induction machine modeling for internal faults simulation", Electric Power Components and Systems, 43(14), pp. 1610–1620, 2015. https://doi.org/10.1080/15325008.2015.1051634

[4] Maanani, Y., Menacer, A., "Modeling and diagnosis of the inter-turn short circuit fault for the sensorless input-output linearization control of the PMSM", Periodica Polytechnica Electrical Engineering and Computer Science, 63(3), pp. 159–168, 2019. https://doi.org/10.3311/PPee.13658

[5] Razik, H. "Modelling of double star induction motor for diagnosis purpose", IEEE International Electric Machines and Drives Conference, 2, pp. 907–912, 2003. https://doi.org/10.1109/IEMDC.2003.1210342

[6] Imaouchen, Y., Alkama, R., Thomas, M. "Bearing fault detection using motor current signal analysis based on wavelet packet decomposition and Hilbert envelope", MATEC Web of Conferences, 20, 03002, 2015. https://doi.org/10.1051/matecconf/20152003002

[7] Lizarraga-Morales, R. A., Rodriguez-Donate, C., Cabal-Yepez, E., Lopez-Ramirez, M., Ledesma-Carrillo, L. M., Ferrucho-Alvarez, E. R. "Novel FPGA-based methodology for early broken rotor bar detection and classification through homogeneity estimation", IEEE Transactions on Instrumentation and Measurement, 66(7), pp. 1760–1769, 2017. https://doi.org/10.1109/TIM.2017.2664520

[8] Benchabane, F., Guettaf, A., Yahia, K., Sahraoui, M. "Experimental investigation on induction motors inter-turns short-circuit and broken rotor bars faults diagnosis through the discrete wavelet transform", Elektrotechnik and Informationstechnik, 135(2), pp. 187–194, 2018. https://doi.org/10.1007/s00502-018-0607-6

[9] Layadi, N., Djerioui, A., Zeghlache, S., Mekki, H., Houari, A., Benkhoris, M. F., Berrabah, F. "New fault tolerant control based on backstepping controller for double star induction machine", Revue Roumaine des Sciences Techniques, Série Électrotechnique et Énergétique, 64(3), pp. 275–280, 2019.

[10] Razik, H., Didier, G., Lubin, T., da Silva, C. R., Mascarenhas, A. W., Jacobina, C. B. "A model of double star induction motors under rotor bar defect for diagnosis purpose", In: 2005 IEEE International Conference on Industrial Technology, Hong Kong, China, 2005, pp. 197–202. ISBN 0-7803-9484-4 https://doi.org/10.1109/ICIT.2005.1600635

[11] Khadar, S., Kouzou, A., Rezzaoui, M. M., Hafaifa, A. "Sensorless control technique of open-end winding five phase induction motor under partial stator winding short-circuit", Periodica Polytechnica Electrical Engineering and Computer Science, 64(1), pp. 2–19, 2020. https://doi.org/10.3311/PPee.14306

[12] Guettab, A., Boudjema, Z., Bounadja, E., Taleb, R. "Improved control scheme of a dual star induction generator integrated in a wind turbine system in normal and open-phase fault mode", Energy Reports, 8, pp. 6866–6875, 2022. https://doi.org/10.1016/j.egyr.2022.05.048

[13] Dehina, W., Boumehraz, M. "Experimental investigation in induction motors using signal processing techniques for early detection of inter-turn short circuit faults", International Journal of Modelling and Simulation, 42(5), pp. 855–867, 2022. https://doi.org/10.1080/02286203.2021.2001635

[14] dos Santos, T., Ferreira, F. J. T. E., Pires, J. M., Damásio, C. "Stator winding short-circuit fault diagnosis in induction motors using random forest", In: 2017 IEEE International Electric Machines and Drives Conference (IEMDC), Miami, FL, USA, 2017, pp. 1–8. ISBN 978-1-5090-4282-1 https://doi.org/10.1109/IEMDC.2017.8002350

[15] Amirouche, E., Iffouzar, K., Houari, A., Ghedamsi, K., Aouzellag, D. "New diagnostic and severity estimation method for inter-turn short fault for dual star permanent magnet synchronous generator", Arabian Journal for Science and Engineering, 47(3), pp. 3573–3581, 2022. https://doi.org/10.1007/s13369-021-06445-2

[16] Chekkal Ait Ouaret, S., Imaouchen, Y., Aouzellag, D., Ghedamsi, K. "A new modeling approach and comprehensive monitoring of electrical faults through spectral analysis in DSIM", Periodica Polytechnica Electrical Engineering and Computer Science, 68(4), pp. 344–355, 2024. https://doi.org/10.3311/PPee.37305

[17] Nounou, K., Charpentier, J. F., Marouani, K., Benbouzid, M., Kheloui, A. "Fault-tolerant control of VSI driven double star induction machine for electric naval propulsion", In: 2018 IEEE International Power Electronics and Application Conference and Exposition, Shenzhen, China, 2018, pp. 1–6. ISBN 978-1-5386-6054-6 https://doi.org/10.1109/PEAC.2018.8590291

[18] Hossine, G., Katia, K. "Analyze and fault diagnosis of double star induction motor using wavelet transformation", Springer International Publishing, 174, pp. 233–242, 2021. https://doi.org/10.1007/978-3-030-63846-7_23

[19] da Silva, C. R., Correa, M. B. R., Jacobina, C. B., Lima, A. M. N., da Silva, E. R. C., Andriamalala, R. N. "A new approach for inter-turn short-circuit detection in six-phase induction motor", In: IECON 2006 – 32nd Annual Conference on IEEE Industrial Electronics, Paris, France, 2006, pp. 4969–4974. ISBN 978-1-5090-9155-3 https://doi.org/10.1109/IECON.2006.347634

[20] Choi, S. D., Akin, B., Rahimian, M. M., Toliyat, H. A., Azadpour, M. "A generalized condition monitoring method for multi-phase induction motors", In:2009 IEEE International Electric Machines and Drives Conference, Miami, FL, USA, 2009, pp. 556–562. ISBN 978-1-4244-4251-5 https://doi.org/10.1109/IEMDC.2009.5075261

[21] Ismail, M. M. "Predictive maintenance based on earlier fault detection of multi-phase induction machines using neural network artificial intelligence techniques", Journal of Engineering Sciences, 41(4), pp. 1612–1636, 2013. https://doi.org/10.21608/jesaun.2013.114886

[22] Taheri, A., Sabouri, M. "Magnetic saturation impacts on fault analysis of squirrel-cage six phases induction motors using winding function approach", International Journal of Engineering, 27(9), pp. 1359–1366, 2014. https://doi.org/10.5829/idosi.ije.2014.27.09c.05

[23] Foito, D., Maia, J., Pires, V. F., Martins, J. F. "Fault diagnosis in six-phase induction motor using a current trajectory mass center", Measurement, 51, pp. 164–173, 2014. https://doi.org/10.1016/j.measurement.2014.02.004

[24] Filippetti, F., Franceschini, G., Tassoni, C., Vas, P. "Recent developments of induction motor drives fault diagnosis using AI techniques", IEEE Transactions on Industrial Electronics, 47(5), pp. 994–1004, 2000. https://doi.org/10.1109/41.873207

[25] MathWorks Inc "MATLAB and SIMULINK, (R2015b)", [computer program] Available at: https://www.mathworks.com/products/matlab.html [Accessed: 30 June 2024]

[26] Prodhan, M. A. I., Yin, X., Kim, S., McClain, C., Zhang, X. "Surface fitting for calculating the second dimension retention index in comprehensive two-dimensional gas chromatography mass spectrometry", Journal of Chromatography A, 1539, pp. 62–70, 2018. https://doi.org/10.1016/j.chroma.2018.01.049